Co-operative Optical and Inverse Synthetic Aperture Radar (ISAR) Systems for High-Resolution In-Orbit Conditional Monitoring of Satellites

Leah-Nani Alconcel and Lily Beesley
School of Metallurgy and Materials, University of Birmingham, UK

Gruffudd Jones, Morgan Coe, and Marina Gashinova
School of Engineering, University of Birmingham, UK

29 August 2025

Abstract

In this work, the concept of cooperative optical and ISAR systems to detect targets and autonomously optimise the conditions for subsequent ISAR image formation during an encounter between two satellites is introduced and explored. The system analysis includes the geometry of the observed satellite (OS), the OS's reflectivity, solar array orientation, solar angle, and the orbital geometries of both OS and monitoring satellite (MS). A wide-angle camera has been identified as a suitable option, and the detection capability of a specific star tracker has been explored. The results show that detection of the OS is possible using the MS optical system at ranges of up to 2,000 km. Coupled with pre-existing ephemeris knowledge of MS and OS positions, this should enable precise MS re-orientation and dual-frequency sub-THz antenna pointing to maximise the number of high-resolution ISAR frames produced at every encounter.

1. INTRODUCTION

Space Domain Awareness (SDA) is essential for space asset security and future operational sustainability of the space environment around Earth and beyond. While ground-based radar and optical sensors observe large volumes of space, in-orbit sensing can achieve close proximity observations, resulting in detailed multi-aspect imagery. This technology can meet the demand for on-orbit inspection, activity monitoring, and fault or anomaly detection, where resident space object (RSO) characterisation with fine resolution (at least 10 cm) is needed to enable feature identification. It is also a capability requirement for in-orbit servicing, assembly and manufacturing (ISAM). A radar technique highly suitable for the provision of high-resolution on-orbit SDA is inverse synthetic aperture radar (ISAR) [1] . The ISAR imaging principle has a number of advantages for imaging highly dynamic objects. It is formed by utilising differential Doppler shifts of different parts of moving objects within the surveillance volume during an observation. The use of auto-focussing algorithms relaxes the requirement on the knowledge of motion parameters, which enables imaging of non-cooperative objects and space debris.

Previous research in this group defined the concept of sub-THz ISAR imagery from space-borne platforms [1, 2]. Generalised scenarios of co- and counter-rotating LEO satellites were considered and initial estimates of ISAR resolution with fixed and tracking antennas were obtained. A dual-band antenna system using two frequencies, 75 GHz and 300 GHz, was investigated for ISAR image formation, which is also used in this study.

In this work, the concept of cooperative optical and ISAR systems to detect targets and autonomously optimise the conditions for ISAR image formation during an encounter between two satellites is introduced. The geosynchronous (GEO) belt is chosen for this study, as it is the location of many high-value space assets. Henceforth, the monitoring satellite bearing the optical and ISAR systems is denoted as MS, while the target satellite at GEO is denoted as the observed satellite, OS.

2. BACKGROUND AND MOTIVATION

While ISAR imagery can provide very fine resolution of an RSO, prepositioning the ISAR beam of the MS on its approach to the OS is challenging due to the uncertainty in the target's true position, posing a risk of mispointing

during the encounter. Here, we consider using on-board optical sensors to provide the required positional information, allowing sufficient time to derive precise orientation data prior to the MS-OS encounter to accurately point the radar antenna.

The MS-OS encounter and dual-frequency antenna system are defined with the following parameters, as in [1]:

1. The maximum closest approach (CA) distance for ISAR image formation is 100 km.
2. The dual-frequency antenna diameter is 30 cm.
3. The dual-frequency antenna beamwidth when operating at 300 GHz is 0.23°.

A short summary of the rationale for using these parameters is given below. The dual-band antenna system uses a steering mechanism to track the OS for the duration of the encounter. The narrow beamwidth of the antenna imposes strict demands on the accuracy of the tracking. The half-power beamwidth (HPBW) of the antenna can be calculated by:

$$\theta \approx 1.22 \frac{c}{f_c D} \tag{1}$$

The $f_c = 300$ GHz operation mode, using an antenna with diameter $D = 30$ cm will have HPBW $\theta = 0.23°$. At 75 GHz, the beamwidth is wider, at 0.92°. The higher frequency band therefore constrains the required pointing accuracy. At a distance of 50 km, the projected width of the 300 GHz beam is 200 metres. In ISAR, the range and cross-range resolutions of an image are given by:

$$\Delta \mathrm{R} = \frac{c}{2B} \tag{2}$$

$$\Delta \mathrm{CR} = \frac{c}{2 f_c \Omega}. \tag{3}$$

where B is the signal bandwidth and Ω is the angular span subtended during the coherent integration interval. The angles required to produce a cm-resolution image at sub-THz frequencies for the OS-MS encounter geometries are small ($< 1°$).

Parametric ISAR image focusing techniques, and non-parametric techniques such as phase-gradient autofocus, rely on the assumption that motion parameters of the target such as radial velocity, acceleration and angular velocity are linear during the coherent integration time. The observation time during the MS-OS encounter is typically on the order of tens of seconds, due to the high relative velocity of the MS and OS. Therefore the coherent integration interval is sufficiently short to avoid non-linear defocusing from higher-order motion terms. Further justifications for designing MS deployment scenarios that produce MS-OS encounters with high relative velocity can be found in [1]. Co-orbiting monitoring spacecraft are impractical platforms for the ISAR sensing system, as these would use similar orbits to the OS and produce MS-OS encounters at low relative velocities.

As an example of a high relative velocity encounter, an MS is placed in an inclined Molniya-type orbit with an apogee near GEO. The MS will have a velocity relative to RSOs in uninclined GEO orbits of 2.82 km/s. This deployment scenario was explored in a previous study [3], and shown in Figure 1. The MS-OS encounter duration at $\leq$ CA is 60 seconds on average, during which ISAR measurements are conducted. A simulated ISAR image at $f_c = 300$ GHz corresponding to this encounter scenario is shown in Figure 2.

The probability of detection of a GEO RSO by an MS deployed in this orbit and using only two-line-elements (TLEs) ephemerides at the maximum CA is established as a starting point for the current study. Literature indicates that the true position of a GEO satellite differs from the TLE-predicted position by 4.0 ± 7.5 km cross-track and 4.9 ± 23 km along track [4]. Using Monte Carlo analysis, the probability of detecting a GEO RSO based on its TLE ephemerides, with an MS payload system consisting solely of a fixed narrow-beam ISAR antenna (0.23°) with a cross-range field of view (FOV) of 400 m at 100 km from the OS, is 0.03%. Figure 3 illustrates these Monte Carlo simulation results.

This result demonstrates that TLE usage alone for narrow-beam antenna pointing will not be sufficient to plan observations of an OS from the antenna-bearing MS. The detection probability could be greatly increased through a combination of acquiring high-precision ephemerides from a commercial provider and using an on-board optical guide camera. The guide camera can also facilitate real-time on-board conjunction analysis with other satellites.

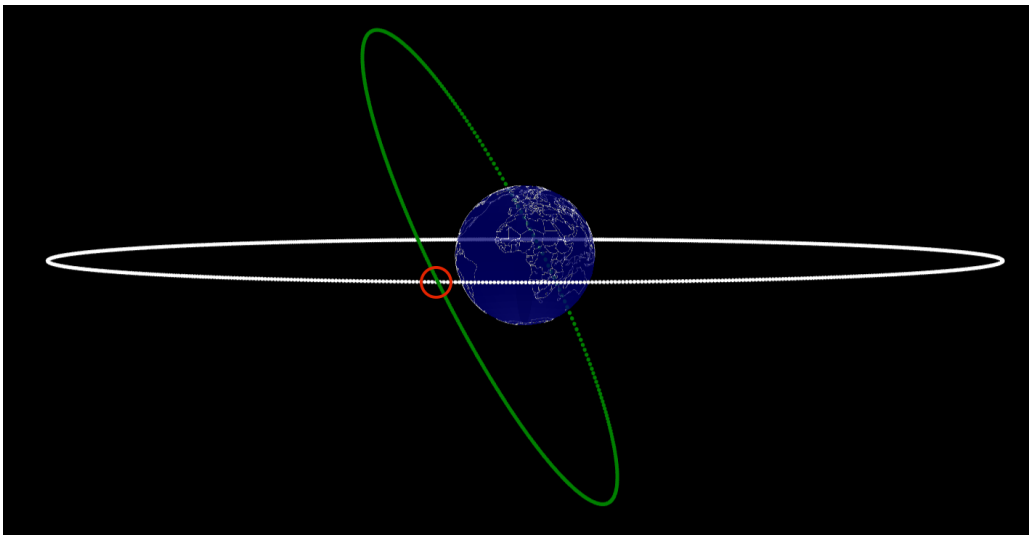

Figure 1: Schematic of an example MS deployment, generated using Ansys STK. (Green: MS, white: OS). The red circle marks the point where an encounter occurs.

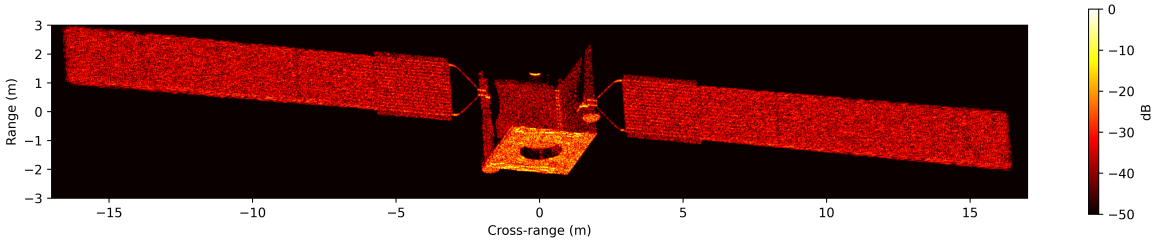

Figure 2: Simulated 300 GHz ISAR image of a large geostationary asset acquired during an encounter in GEO. Bandwidth $B = 7.5$ GHz, with range and cross-range resolutions: 2 cm.

3. SIMULATION METHODOLOGY

The pointing of the radar instrument in anticipation of ISAR imaging will be provided by a combination of antenna alignment and the MS attitude control systems. It is assumed that the required re-orientation following the determination of the OS position will require up to 10 minutes. Given the typical relative velocities needed to form ISAR imagery, this requires the optical system to sense the position of the OS at a distance of 2,000 km prior to CA.

At this distance, to achieve a 99.7% detection rate, the camera's sensor must be capable of observing $\pm 3\sigma$ around the TLE-derived predicted position, where σ is the along-track error in the TLE. This equates to a 4° FOV, which is significantly wider than the FOV typically used by traditional on-board space situational awareness (SSA) cameras. Star trackers have a wide-angle FOV while being compact, making them well-suited when considering size, weight and power (SWaP) requirements. The camera used in these simulations is the ECAM-M50, a monochrome CMOS camera weighing 590 g, with a power consumption of 1 W when idle and 1.6 W when imaging [5]. Its optical specifications include a minimum FOV of $4^\circ \times 5^\circ$, a pixel resolution of 1944×2592 pixels, a bandpass of 350-750 nm, a quantum efficiency (QE) greater than 62% at 550 nm, and 9 e- temporal noise. With these specifications, the OS will appear as a single illuminated pixel in the optical sensor's field of view, serving solely for positional tracking, and at no point will the OS's features be resolvable in the guide camera.

To determine the apparent brightness of the satellite as observed by the guide camera, it is necessary to model the light received by the OS from the Sun and then the light reflected from the OS to the MS guide camera. For this analysis, the OS-centred frame is used.

To accurately model the reflected light, the geometry, orientation, and materials of the OS must be representative of

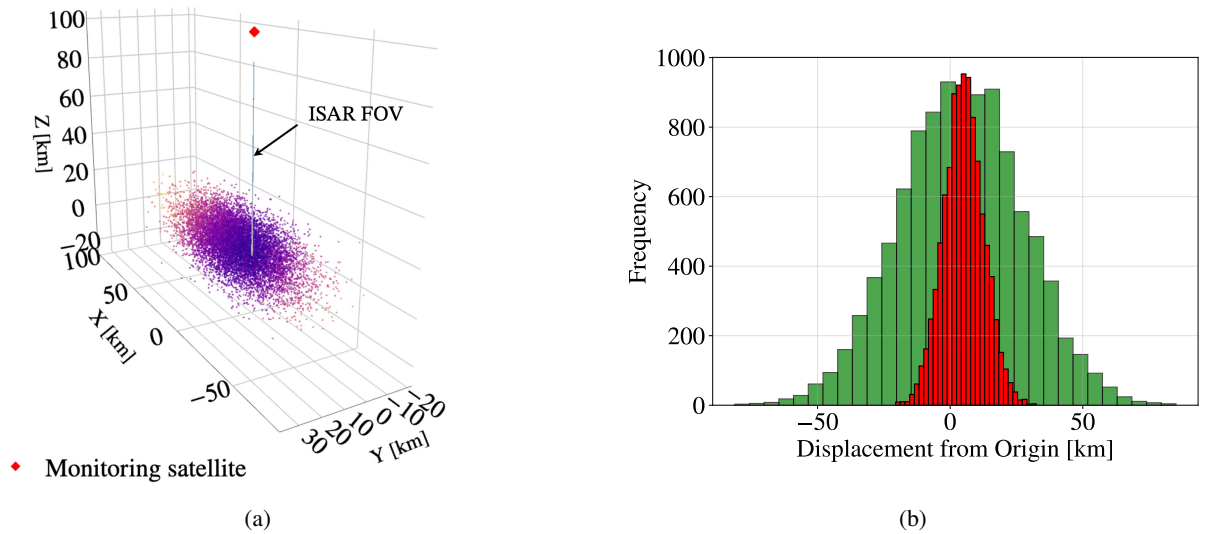

(a) (b)

Figure 3: Analysis of TLE-derived displacement distribution. (a) Scatter distribution of the displacement of the OS in GEO from TLE-derived position based on statistics from [4]. Each dot represents a single realization generated using Monte Carlo simulation. (b) Histogram showing the distribution of along-track (green) and cross-track (red) displacements.

a GEO satellite. For this study, the OS was modelled after Skynet-5D, whose bus can be approximated as a cube where the front of the cube is nadir-facing and each side measures 3 m. The solar arrays are modelled as two 15 m by 3 m planar solar surfaces which rotate to face the Sun. The reflective properties of both aluminium (bus) and solar surfaces (arrays) are modelled using the bidirectional reflectance distribution function (BRDF). As well as being computationally efficient, the simplicity of this model enables a first approximation of the received light. However, as it is a low-fidelity representation there will be no higher-order fluctuations in the reflected light.

The ray-tracing model follows the methodology described in [6], where the satellite is considered as a combination of N_S surfaces, with the scattered sunlight from each surface calculated individually. The flux from the Sun is calculated for each surface based on the incident angle between the sunlight and each surface. The amount of solar flux subsequently scattered from OS and MS, I_{MS}, is calculated by:

$$\begin{aligned} I_{MS} &= I_{Sun} \sum_{s=1}^{N_S} G_s(Sun \rightarrow MS), \\ G_s(Sun \rightarrow MS) &= \frac{A_s f_s(\hat{v}_{Sun\rightarrow OS}, \hat{v}_{OS\rightarrow MS}) N_S}{\|\mathbf{x_{obs}} - \mathbf{x_{sat}}\|^2}, \\ N_S &= (\hat{n}_s \cdot \hat{v}_{Sun\rightarrow OS})(\hat{n}_s \cdot \hat{v}_{OS\rightarrow MS}), \end{aligned} \tag{4}$$

where A_s, f_s, and $\hat{n}_s$ represent the surface area of each surface, the BRDF, and the normal vector of each surface, respectively. I_{Sun} is the solar flux received by the OS, which is 1360 W/m^2. The outgoing vector, $\hat{v}_{Sun\rightarrow OS}$, from the Sun to the OS, is modelled by varying the solar angle from 0° to 360° in the equatorial plane. The incident vector, $\hat{v}_{OS\rightarrow MS}$, from the OS to the MS, is calculated using both satellites' orbital geometry.

As I_{MS} is given in W/m^2, the received intensity in the guide camera will be I_{MS} multiplied by the aperture size. The number of photons (N_p) received over the camera's integration time can be derived from the following relationship:

$$I_{MS} = A \cdot N_p \cdot \frac{hc}{\lambda} \cdot \tau, \tag{5}$$

where A is the area of the camera aperture, h is Plank's constant, c is the speed of light, λ is the central wavelength (550 nm), and τ is the integration time. For ECAM, τ is 0.36 seconds. This also assumes a gain of 1. The camera's response can be calculated by determining the number of electrons released from the detector, which is given by $N_e = N_p \cdot QE$.

4. SIMULATION RESULTS

4.1 Brightness as a Function of Solar Angle

Figure 4a shows the results from the optical brightness simulations, showing the variation in optical brightness as a function of solar angle and the distance between OS and MS. For this deployment of the MS and model of the OS, it can be seen that 25% of the time there will be no light reflected from the OS into the guide camera, which occurs when the OS is between the MS and the Sun. This is indicated by the black regions in the two plots of Figure 4. The plot shows that the OS is brightest between solar angles of 0° and 180°, specifically at 90°, corresponding to measurements where the solar panels are facing directly towards the MS. A second, less intense peak occurs at 315° caused by scattering from only one side of the OS's bus. Both of these peaks in maximum brightness are observed in Figure 5.

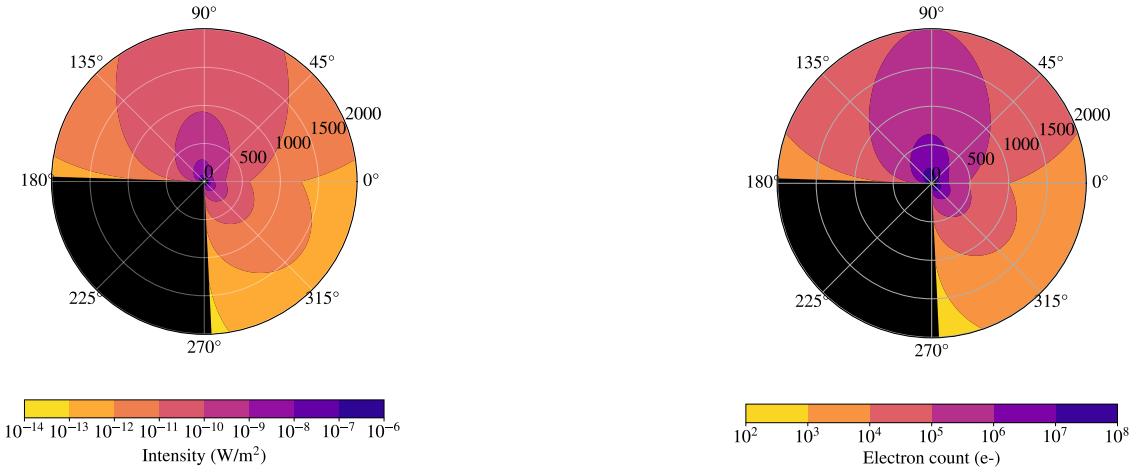

(a) Intensity of OS.

(b) Camera response to OS.

Figure 4: The received flux and camera response over a 0.36 second exposure as a function of solar angle and distance between OS and MS, where 0° is when the Sun is directly behind the Earth.

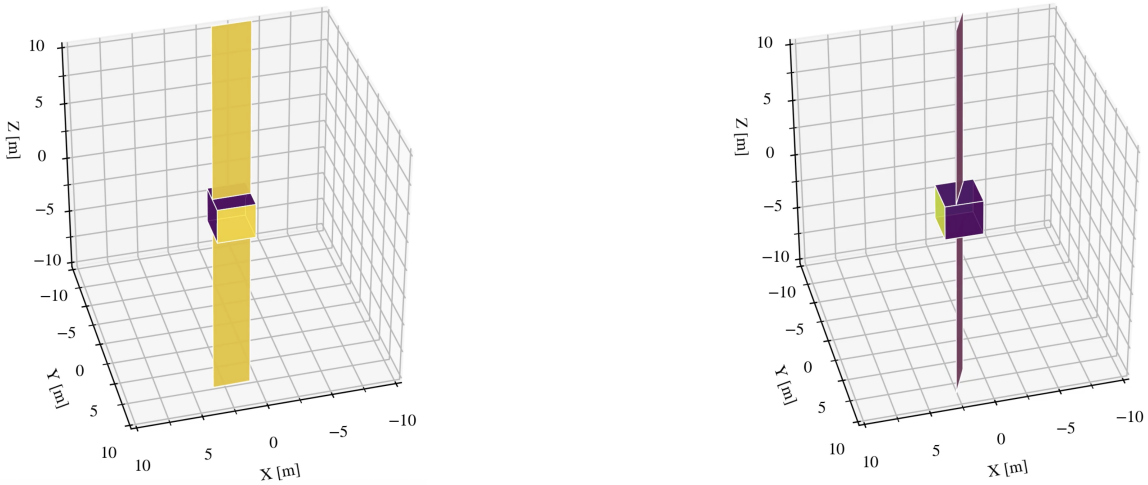

Figure 5: The observed brightness of OS at 180° (left) and 315° (right) solar angles from the perspective of MS. Yellow surfaces indicate solar illumination and blue surfaces have no illumination.

Figure 4b shows the camera's response to the incident photons over a 0.36 second exposure. ECAM-M50 reaches saturation at 7,000 e-, allowing the OS to be observed during most instances between 0° and 180°. In instances of saturation, the gain or integration time may be reduced to prevent blooming and to limit background brightness. The camera has a lower response when illuminated between 270° and 0° and may require an increased integration time or gain to observe the OS if approaching at these solar angles. This result shows that while the guide camera can identify the OS's position from 2,000 km for a majority of solar angles, caution is needed when scheduling encounters since for ∼25% of solar angles the guide camera will not be able to sense the position of the OS and thus target acquisition may not be possible.

4.2 Satellite brightness against background stars

To establish if the brightness of the OS is such that the object is distinguishable from the background starts, both the relative brightness and density of the background stellar field needs to be assessed. To do this, the line-of-sight directional vector from MS to OS was converted to right ascension and declination coordinates in the International Celestial Reference System (ICRS). These values are used to query the corresponding sky region through the VizieR catalog service to retrieve background star positions and G-band flux value (FG parameter) [7]. The FG parameter was chosen as it can be considered representative as its broad spectral range is similar to the spectral range of ECAM's sensor.

Since the FG parameter is given in electrons per second, it is necessary to convert this to incident photons per metre per second in order to remove any instrumental dependencies. This was done by dividing by the average quantum efficiency of Gaia's G-band sensor, which is ∼55%, and normalising over the telescope aperture which has a collecting area of 1.45 m × 0.50 m [8].

The positions of the OS and the MS were interpolated to match the time step of the camera's frames with an integration time of 0.36 seconds. For each frame, a field-of-view mask was applied to select stars within the observing region. The stars' apparent motion due to spacecraft movement was calculated by applying the relative shift in right ascension and declination to the stellar positions. This apparent motion over the exposure duration results in trails across the sensor, which appear as lines of illuminated pixels extending from each star's initial position to its final position during the sensor's exposure.

As discussed in the previous section, the brightness of OS is sufficient to saturate the sensor and cause blooming. Although the process of blooming is specific to each sensor, typically CMOS sensors bloom radially with charge losses between pixels. In simulation, without detailed knowledge of the specific sensor characteristics, it is assumed that charge transfer is lossless as a worst-case scenario. This was emulated by allowing saturated pixels to spill electrons into the neighbouring pixels, until the total integrated charge across all affected pixels equals the original electron count. As per ECAM's specifications, 9 e- of read noise was added to each exposure.

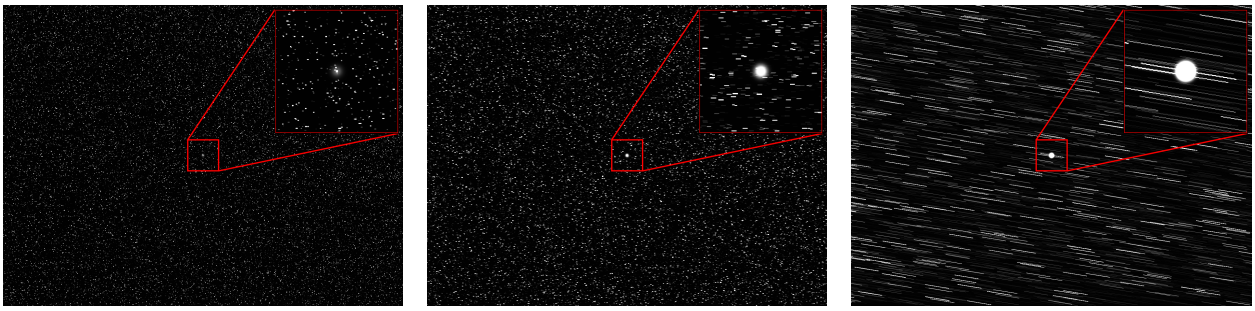

Figure 6: Simulated frames at distances of 2000 km, 1000 km and 100 km (from left to right) at a solar angle of 90°.

Figure 6 shows the outputs from the simulation at three different ranges. At this illumination angle, the OS is clearly distinguishable from the background stars at a distance of 2000 km. Furthermore, for real-time imaging there is relative motion between the OS and the background stellar field in consecutive frames allowing for object identification. The background stars are also sufficiently visible that astrometry can be easily performed. Significant blooming is exhibited on approach to the OS as the received photon flux from OS saturates the sensor. This effect can be lessened by reducing the integration time or gain.

5. SIMULATION VALIDATION

The brightness simulation developed in this work can be validated against real observational data to ensure model accuracy. However, due to the lack of available optical data for Skynet-5D, validation was performed by making comparisons with Starlink light curves. These were obtained from the Mini-Mega-TORTORA database which includes light curves for over 9,000 objects [9].

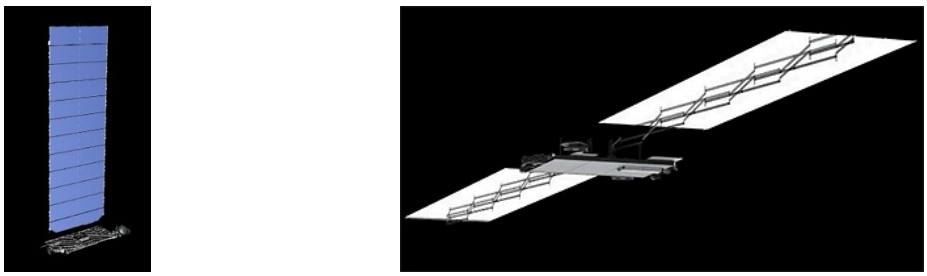

Figure 7: Renders of Starlink v1.5 (left) and Starlink v2.0-mini (right). Credit: SpaceX.

Starlink satellites function as an appropriate validation target due to their well-document geometries in [10] and extensive observation datasets, constituting up to 65% of all active satellites [11]. Two versions of Starlink satellites are modelled here (Figure 7), Starlink v1.5 and Starlink v2.0-mini, which together comprise of a majority of Starlink satellites.

The Starlink v1.5 was modelled in its shark-fin configuration using four surfaces, two 1.8 m $\times$ 3.7 m representing the satellite bus and two 8.9 m $\times$ 3.7 m representing the structure for the solar array. The satellite bus normal was initially oriented toward nadir, while the solar array was positioned perpendicular to the velocity vector. Surface normals to each pair of surfaces were configured as antiparallel to ensure reflectance from both faces of each structure. The bus and the solar panel were modelled as orthogonal with respect to each other. The BRDF characteristics were assigned as follows: aluminium for the satellite bus surfaces, solar panel material for the satellite bus facing solar array surface, and aluminium for the rear solar array surface.

Starlink v2.0-mini was modelled using an analogous method but with a flatter configuration when compared to the v1.5. The satellite bus was formed of two 4.1 m $\times$ 2.7 m surfaces and the two solar panel structure as 4.1 m $\times$ 12.8 m surfaces. All structural components were assumed to be coplanar, with the lower surface facing nadir. BRDF characteristics were assigned as aluminium for all surfaces, with the exception of the zenith-facing solar array surface, which was modelled as solar panel material.

Data were selected from the comparison for Starlink-5670 and Starlink-31464, which were observed on the 4th of May 2025. The positional data of the two spacecraft were accessed using historical TLEs from Space-Track and propagated to the observation time using SGP4 [12]. The observer position was set to the coordinates of the Mini-Mega-TORTORA telescope at the Special Astrophysical Observatory (SAO) in the Russian Caucasus (43.65°N, 41.44°E, 2070 m elevation).

Since attitude information for Starlink satellites is not publicly available, light curves were generated for each Starlink version by varying the spacecraft's pitch and yaw through $\pm 10^{\circ}$ in both axes to identify the optimal attitude configuration that best matched the observed data.

Figure 8 compares the measured light curve with the simulated light curve for both Starlink v1.5 and v2.0-mini. It can be seen that the received intensity is the same order of magnitude for both spacecraft. As expected, the simulation does not capture small scale intensity fluctuations, which can be primarily attributed to the simplified representation of both spacecraft's geometries. The difference between simulated and observed optical brightness is expected to increase for more structurally complex spacecraft as the assumption of the simplified geometry is no longer valid.

Additionally, the resolution of the available BRDF measurements does not capture highly specular reflections, and the simulation does not account for structural occlusion effects or self-shadowing between satellite components. Despite this, this validation demonstrates that the simulation provides a reliable first-order approximation of the observed

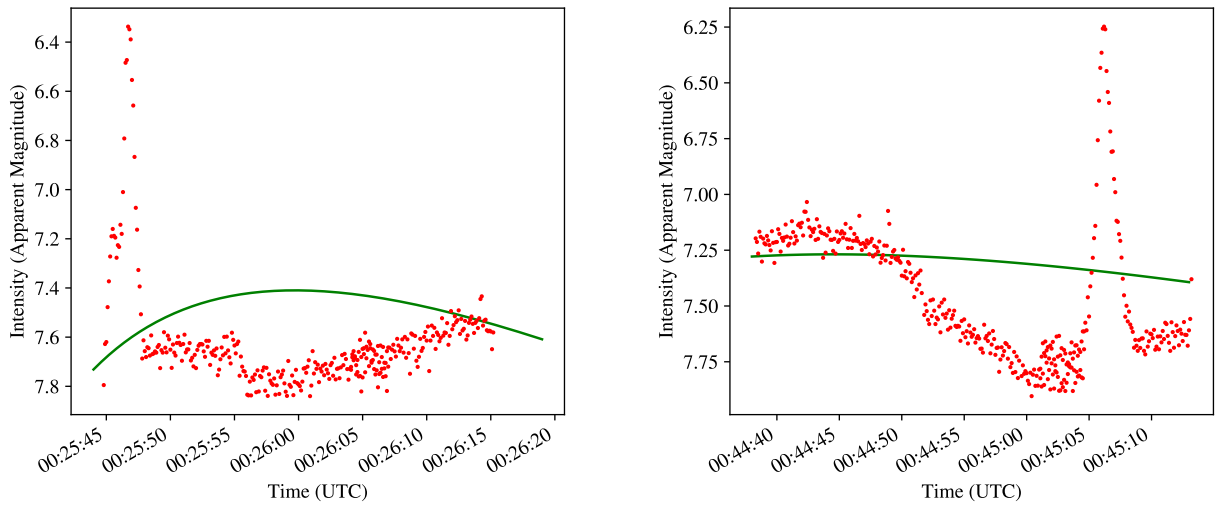

Figure 8: Comparisons between the simulated light curves (green) and the measured light curves (red) for Starlink v1.5 (left) and Starlink v2.0-mini (right).

optical brightness.

6. CONCLUSION

The requirements of a cooperative optical guidance system to be used in conjunction with a dual-frequency, sub-THz ISAR antenna for high-resolution conditional monitoring of GEO satellites have been investigated. A wide-angle camera has been identified as a suitable option, and the detection capability of a specific star tracker has been explored.

The optical brightness of the satellite has been assessed to ensure that the guide camera's sensor can detect the position of the OS. Through this analysis, it has been found that for the Molniya-type deployment of the MS, there is no light being reflected from the OS to the MS for 25% of solar angles. Additionally, the optimal solar angle for observations in the guide camera is 180° where the solar array of the OS faces directly toward the MS. It has also been shown that using ECAM-M50, the OS will be bright enough to saturate the camera sensor at 40% of solar angles, in which case a reduced integration time or lower gain can be applied. It was also found that at 180°, the OS is bright enough for it to be distinguishable from the background stellar field.

With this understanding of OS brightness, clear identification of the OS within the TLE-defined region and its location can be made whilst on orbit, to supplement prior knowledge of its trajectory from the available ephemeris. The OS solar array will be oriented in a specific direction based on this brightness. Adjustments to the MS attitude and steering the dual-frequency sub-THz ISAR antenna orientation can be performed to maximize the total imaging time and number of ISAR images during the MS-OS encounter.

To validate the simulation work, comparisons between the simulation and on-sky observations were conducted using Starlink-v1.5 and v2.0. The simulation gave a consistent first-order approximation of the expected observed apparent magnitude. Small-scale intensity fluctuations were not reproduced due to both simplified spacecraft geometry and low-resolution BRDFs. Despite these limitations, this work demonstrates applicability beyond ISAR systems, offering a framework for cooperative optical guidance that can improve target acquisition and tracking for any narrow-field space-based SDA instrument.

Acknowledgement: Funding from the UK Space Agency's Enabling Technologies Programme (ETP2-028) is gratefully acknowledged. The results presented in this paper make use of Python [13], NumPy [14], Matplotlib [15], Plotly [16], and Pandas [17].

7. REFERENCES

[1] Emidio Marchetti et al. “Space-Based Sub-THz ISAR for Space Situational Awareness-Concept and Design”. In: *IEEE Transactions on Aerospace and Electronic Systems* 58.3 (2022), pp. 1558–1573. ISSN: 15579603. DOI: 10.1109/TAES.2021.3126375.

[2] Emidio Marchetti et al. “Space-Based Sub-THz ISAR for Space Situational Awareness - Laboratory Validation”. In: *IEEE Transactions on Aerospace and Electronic Systems* 58.5 (2022), pp. 4409–4422. DOI: 10.1109/TAES.2022.3160985.

[3] Gruffudd Jones et al. “Strategies for Monitoring of Assets in Geosynchronous Orbit (GEO) Using Space-Based Sub-THz Inverse Synthetic Aperture Radar (ISAR)”. In: *IEEE Trans. Radar Syst.* 3 (2025), pp. 656–667.

[4] Carolin Früh and Thomas Schildknecht. “Accuracy of Two-Line-Element Data for Geostationary and High-Eccentricity Orbits”. In: *Journal of Guidance, Control, and Dynamics* 35.5 (Sept. 2012), pp. 1483–1491. ISSN: 0731-5090. DOI: 10.2514/1.55843. URL: https://arc.aiaa.org/doi/10.2514/1.55843.

[5] Malin Space Science Systems. *ECAM-C50 M50*. https://www.msss.com/files/ECAM-C50_M50.pdf. Accessed: 2024-12-19. 2024.

[6] Forrest Fankhauser, J. Anthony Tyson, and Jacob Askari. “Satellite Optical Brightness”. In: *The Astronomical Journal* 166.2 (2023), p. 59. ISSN: 0004-6256. DOI: 10.3847/1538-3881/ace047.

[7] Adam Ginsburg et al. “astroquery: An Astronomical Web-Querying Package in Python”. In: *The Astronomical Journal* 157.3 (Jan. 2019), p. 98. ISSN: 1538-3881. DOI: 10.3847/1538-3881/aafc33. URL: https://iopscience.iop.org/article/10.3847/1538-3881/aafc33http://arxiv.org/abs/1901.04520http://dx.doi.org/10.3847/1538-3881/aafc33.

[8] J. H. J. de Bruijne. “Science performance of Gaia, ESA’s space-astrometry mission”. In: *Astrophysics and Space Science* 341.1 (Sept. 2012), pp. 31–41. ISSN: 0004-640X. DOI: 10.1007/s10509-012-1019-4. URL: http://link.springer.com/10.1007/s10509-012-1019-4.

[9] S. Karpov et al. “Massive photometry of low-altitude artificial satellites on Mini-Mega-TORTORA”. In: *Revista Mexicana de Astronomia y Astrofisica Conference Series*. Vol. 48. Revista Mexicana de Astronomia y Astrofisica Conference Series. Dec. 2016, pp. 112–113.

[10] SpaceX. *Re: IBFS File Nos. SAT-LOA-20200526-00055 and SAT-AMD-20210818-00105. Exhibit B. Satellite dimensions and DAS outputs*. Retrieved January 21, 2023. 2022.

[11] David Vallado et al. “Revisiting Spacetrack Report #3”. In: *AIAA/AAS Astrodynamics Specialist Conference and Exhibit*. American Institute of Aeronautics and Astronautics, 2006. DOI: 10.2514/6.2006-6753. URL: http://dx.doi.org/10.2514/6.2006-6753.

[12] 18th Space Defense Squadron, U.S. Space Force. *Space-Track: Space Surveillance Network Data*. Orbital data repository. Accessed: [DATE]. 2023. URL: https://www.space-track.org.

[13] Guido Van Rossum and Fred L Drake. *Python 3 Reference Manual*. Scotts Valley, CA: CreateSpace, 2009. ISBN: 1441412697.

[14] Charles R. Harris et al. “Array programming with NumPy”. In: *Nature* 585.7825 (2020), pp. 357–362. ISSN: 14764687. DOI: 10.1038/s41586-020-2649-2. URL: http://dx.doi.org/10.1038/s41586-020-2649-2.

[15] John D. Hunter. “Matplotlib: A 2D Graphics Environment”. In: *Computing in Science & Engineering* 9.3 (2007), pp. 90–95. ISSN: 1521-9615. DOI: 10.1109/MCSE.2007.55. URL: http://ieeexplore.ieee.org/document/4160265/.

[16] Plotly Technologies Inc. *Collaborative data science*. 2015. URL: https://plot.ly.

[17] Wes McKinney. “Data Structures for Statistical Computing in Python”. In: *Proceedings of the 9th Python in Science Conference*. Vol. 1. Scipy. 2010, pp. 56–61. ISBN: 0440877763224. DOI: 10.25080/majora-92bf1922-00a.